Accelerated Dynamic MRI using Adaptive Signal Models

Sajan Goud Lingala[1] and Mathews Jacob[2]

[1]Department of Electrical Engineering, University of Southern California, Los Angeles, USA
[2]Department of Electrical and Computer Engineering, University of Iowa, Iowa city, USA

March 19, 2015

0.1 Introduction

Dynamic MRI (DMRI) involves imaging physiological processes that are evolving in time. It is central to several research and clinical applications including cardiovascular, pulmonary, abdominal, flow, and vocal tract imaging. The utility of competing methods such as computed tomography (CT) are often prohibitive in dynamic imaging due to the high doses of ionizing radiation. In addition, the ability of MRI to provide unique contrast and functional information distinguishes itself from other modalities in several of these applications.

The main challenges faced by DMRI can be attributed to the slow acquisition nature of MRI, which often results in undesirable tradeoffs betweens spatial resolution, temporal resolution, and number of slices that can be acquired. The classical solutions in some DMRI applications such as cardiac cine imaging include cardiac gating to exploit the periodicity of cardiac motion and breath-holding to eliminate respiratory motion. However, gating is often unreliable in arrhythmia patients, due to high variability in the heart-rates, and can lead to missed triggers. In addition, many subjects cannot tolerate the long breath-hold durations that are needed to achieve high spatio-temporal resolutions that are needed in many applications. Besides, the need for intermittent pauses for the subjects to recover often results in long scan times, which affects patient comfort and throughput. Recently, several researchers have introduced accelerated acquisition schemes that exploit the advances in parallel receive coil technology to improve DMRI. Similarly, the use of compressive sensing to static and dynamic MRI has been an active research area with lot of important contributions, which are covered in detail in the earlier chapters.

In this chapter, we focus on recent advances in image representations that can adapt to the data (data-dependent representations), thus enabling the exploitation of the redundancy in the data. Since these adaptive representations are considerably more efficient in representing the dynamic signal, they provide improved reconstructions over classical linear and compressed sensing methods that rely on pre-determined basis sets (e.g. Fourier/Wavelet). We also highlight explicit and implicit motion compensation strategies to further improve DMRI reconstruction in the presence of significant inter-frame motion. These methods have the potential to enable ungated and free breathing three-dimensional acquisitions, which can improve the workflow in several DMRI applications such as cardiac, pulmonary imaging. While we have made every attempt to provide a good overview of the field, it is by no means comprehensive; the contents of the chapter are certainly biased by our own research interests.

The chapter is organized as follows. We will start with a brief review of gated and breath-held acquisitions, followed by classical linear and compressed sensing methods. We then introduce blind linear (low rank) and blind compressed sensing methods that learn the representation from the data itself. The later sections describes deformation compensation schemes that can be combined with compressed sensing and low-rank methods, which is followed by manifold models that are also learned from the data.
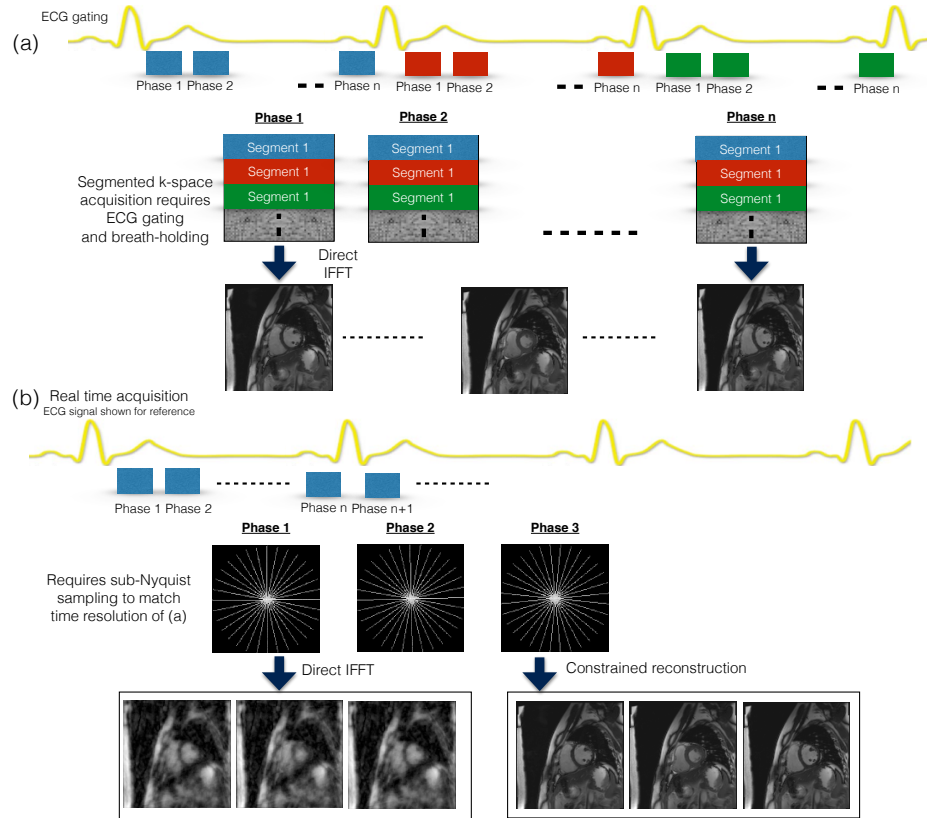
Figure 1: Segmented versus Real time acquisitions: Segmented acquisitions rely on ECG gating signals and subjects ability to maintain perfect breath-holding to fill the k-space of every cardiac phase across several heart beats. Real time acquisitions designed to match the spatio-temporal resolutions of segmented acquisitions attempts to recover the underlying dynamic images from severely sub-sampled k-space measurements.

0.2 Gated and real time acquisitions in DMRI

The MRI data acquired from a static object can be modeled as the spatial Fourier transform (k-space) samples of the object that is support limited in space (often denoted as $\mathbf{r}\epsilon(x, y, z)$). The classical approach is to choose the spacing between k-space samples according to Nyquist sampling rate to avoid alias artifacts, while the extent of k-space coverage determines the spatial resolution of the reconstructed image. In dynamic imaging, one can view the signal as a support limited signal in space and temporal frequency (f); the reconstruction of the signal thus involves the recovery of a finitely supported signal in the $\mathbf{r} - f$ (or popularly termed as $x - f$) domain from its Fourier samples in the complementary domain ($k - t$ space). Since MRI is a slow imaging modality, the number of samples that can be acquired in a finite time is limited; this often results in practical limitations on the achievable spatio-temporal resolution. In a few applications such as cardiac functional cine imaging, and coronary artery imaging, one can use gating signals (such as electro-cardiogram (ECG), or pulse trigger signals) to over come the slow MRI encoding process (see Figure 1). Specifically, assuming the heart to be at the same position at each heart beat, the measurements from different heart beats are stitched together to obtain fully sampled k-space data. This approach is only successful if the subject holds his breath; the motion will be modulated by respiratory motion in the absence of breath-holding. The maximum achievable spatio-temporal resolution is thus limited by the duration of breath-hold.

While ECG gating and breath-holding is the first choice for functional cine imaging in the clinic, this approach has a few practical challenges. Firstly, ECG triggering is unreliable in the presence of high field strengths [1], and while imaging subjects with arrhythmia. Secondly, long breath hold demands cannot be tolerated by a wide range of patient population such as those with compromised pulmonary function, and also limits its utility in imaging pediatric subjects. Besides, the use of this technique to image multiple slices often requires long gaps between acquisitions to allow the subjects to recover from breath-holding, resulting in long acquisition times. In addition, the slices that are acquired from multiple breath-holds may not be perfectly aligned, making it difficult to quantify the data. ECG gating is also employed in applications such as myocardial first pass perfusion imaging, where one is interested in the temporal changes in image contrast due to the passage of a bolus of contrast (e.g. gadolinium). The gating is used to capture the same cardiac phase (usually the diastole phase) across multiple beats. The signal changes due to the passage of the contrast agent is quantified in the regions of the myocardium, to detect abnormalities in myocardial perfusion. Since the diastole duration is limited, the spatial resolution and the number of slices that can be covered is highly restricted in first pass myocardial perfusion MRI.

Most of the current methods rely on fast imaging methods to freeze cardiac/respiratory motion. Common approaches include fast-scan acquisition [2, 3], parallel imaging [4, 5], and their combination with non-Cartesian trajectories [3, 6]. Non-Cartesian trajectories are preferred in this context due to

their superior time efficiency, and robustness to motion artifacts in comparison to Cartesian trajectories, as demonstrated by their early use in several real time studies including imaging the vocal tract during speech production [7, 8], flow imaging [9, 10], and cardiac functional imaging [11, 12]. Despite these advances, the quest for higher spatio-temporal resolutions in real time MRI, that can match the image quality of gated & breath-held acquisition still remains. The recovery of images from highly under-sampled k-space data by exploiting the redundancy in the data has been an active research area; these methods have the potential to overcome the above challenges in both real time and gated acquisitions.

0.3 Recovery from under sampled measurements: problem formulation

As described in previous sections, the reconstruction of the spatio-temporal object from under-sampled $k-t$ space measurements can greatly improve the trade-offs between resolution and coverage in DMRI. We denote the spatio-temporal signal as $\gamma(\mathbf{r}, t)$, where $\mathbf{r} = (x, y, z)$ is the spatial location and t denotes time, and the discretized version is expressed by the N-dimensional vectors:

$$\mathbf{q}_i = [\gamma(\mathbf{r}_i, t_0), \gamma(\mathbf{r}_i, t_1), .., \gamma(\mathbf{r}_i, t_{N-1})]^T; i = 0, .., M-1;$$

where M, and N are respectively the total number of voxels per time frame, and the total number of time frames.

The DMRI measurements corresponding to the noisy samples of the signal in $k - t$ space can be expressed as:

$$\mathbf{b}(k_\mathbf{r}, t_i) \quad = \quad \int_\mathbf{r} \gamma(\mathbf{r}, t_i) \exp\left(-j k_\mathbf{r}^T \mathbf{r}\right) d\mathbf{r} + \mathbf{n}(k_\mathbf{r}, t_i); \tag{1}$$

Here, $(\mathbf{k_r}, t_i)$ indicates the ith sampling location in the $k_\mathbf{r} - t$ space, and $\mathbf{n}$ denotes additive noise in the $k_\mathbf{r} - t$ space.

An acquisition with multiple coil elements modifies Eq.(1) to,

$$\mathbf{b}_l(k_\mathbf{r}, t_i) \quad = \quad \int_\mathbf{r} c_l(\mathbf{r}, t_i) \gamma(\mathbf{r}, t_i) \exp\left(-j k_\mathbf{r}^T \mathbf{r}\right) d\mathbf{r} + \mathbf{n}(k_\mathbf{r}, t_i); l = 1, 2, ...L; \tag{2}$$

where $c_l(\mathbf{r}, t_i)$ denotes coil sensitivity profiles dependent both on space and time.

The expression in Eq.(2) can be rewritten in the vector form as

$$\mathbf{b} = \mathcal{A}(\gamma) + \mathbf{n}; \tag{3}$$

where, the operator $\mathcal{A}$ models for the coil sensitivity encoding as well as Fourier encoding on a specified sampling trajectory (eg. Cartesian, or non-Cartesian). The goal of accelerated DMRI is to recover the spatio-temporal signal (γ) from the under sampled $k - t$ measurements ($\mathbf{b}$).

Global signal model $\gamma(\mathbf{x},t)=\sum_{i=1}^{R} \underbrace{u_i(\mathbf{x})}_{\text{model coeffs.}} \underbrace{v_i(t)}_{\text{temporal bases}}$	Type of temporal basis functions	Number of temporal basis functions	Are model coefficients sparse?	Requirement of Low resolution training data	k-t sampling requirements	Reconstruction
Linear models Ex: DIME, UNFOLD, k-t BLAST	Exponential	Few < N	No	Yes	Coherent	Linear
Blind linear models Ex: PSF, k-t PCA, IRPF, k-t SLR	Learnt	Few < N	No	Yes	Coherent	Linear
				(When posed as low rank matrix recovery)		
				No	Incoherent	Non-linear
Compressed Sensing Ex: k-t FOCUSS, k-t SPARSE	Pre-determined	Many; from an Over-complete dictionary	Yes	No	Incoherent	Non-linear
Blind Compressed Sensing	Learnt	Many; from an Over-complete dictionary	Yes	No	Incoherent	Non-linear

Figure 2: Several spatio-temporal models in DMRI can be interpreted as variants of the general partial separability model (PS), where a single global model is used to model the voxel time profiles (Eq.(4)).

0.4 Accelerated DMRI using linear models and compressed sensing

Several spatio-temporal models that utilize a single global signal model to represent the voxel time profiles $\gamma(\mathbf{r},t)$ can be interpreted by the general partial separability (PS) model proposed by Liang et. al [13]. The PS model represents the dynamic signal, $\gamma(\mathbf{r},t)$ as:

$$\gamma(\mathbf{r},t) = \sum_{i=1}^{R} \gamma_i(\mathbf{r},t) = \sum_{i=1}^{R} u_i(\mathbf{r})v_i(t); \tag{4}$$

where R denotes the total number of basis functions (or the model order), and u_i denotes the model coefficients. The above decomposition $\gamma_i(\mathbf{r},t)$ are separable functions of $\mathbf{r}$, and t; ie they can be factored as a product of the spatial model coefficients $u_i(\mathbf{r})$ and the temporal basis functions $v_i(t)$.

As depicted in Fig.(2), several spatio-temporal model based DMRI schemes have evolved based on the choices in Eq.(4) including the type, and number of temporal basis functions, constraints on the model coefficients, use of low resolution training data, type of $k-t$ sampling, and the reconstruction algorithm. In the sections to follow, we will discuss the categories highlighted in Fig.(2) .

0.4.1 Linear models

To the best of our knowledge, the first adaptive DMRI linear model was proposed by Liang et.al, which was termed as dynamic imaging by model estimation
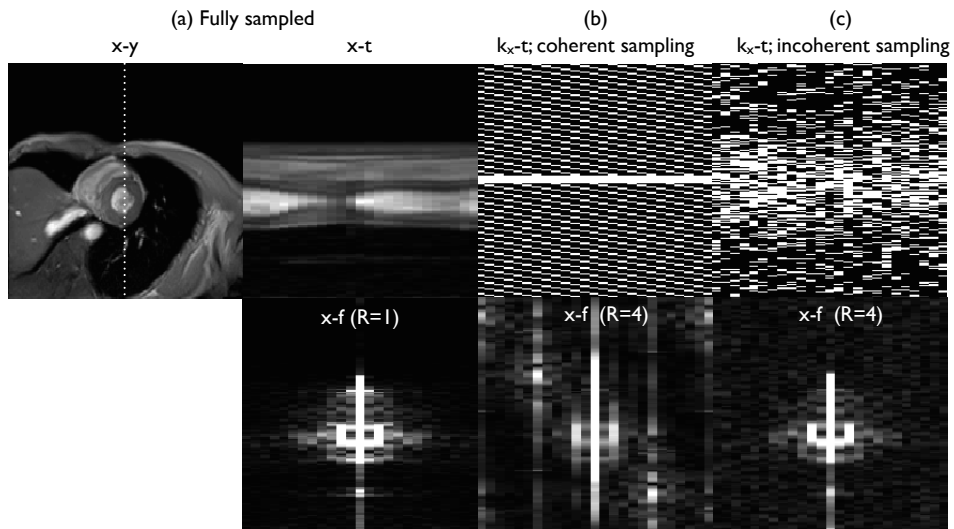
Figure 3: Demonstration of aliasing with coherent and incoherent $k-t$ sampling of a cardiac cine dataset: The spatial-spectral $(x-f)$ profile of the fully sampled cardiac cine dataset has very few non-zero components, and depicts a compact support in the $x-f$ space. Regular (coherent) $k-t$ under sampling results in coherent overlaps of the $x-f$ signal (b); the linear models decouples these coherent artifacts with prior knowledge of the spatial-spectral support from low resolution training data, as noted by full sampling of the low spatial frequencies in (b) . Incoherent k-t sampling (c) is employed by non-linear models such as compressed sensing. Note the aliasing in the $x-f$ space is now incoherent and appears as noise, which are denoised by an iterative CS algorithm, which enforces sparsity in the $x-f$ space subject to consistency with the acquired data.

(DIME) [14]. DIME focusses on the recovery of a periodic signal γ as a linear combination of few exponential temporal basis functions:

$$\gamma(\mathbf{r}, t) = \sum_{i=1}^{R} u_i(\mathbf{r}) e^{j2\pi f_i t}; R < N \qquad (5)$$

The frequencies f_i in the above periodic signal can be determined by using a low spatial but high temporal resolution DMRI dataset; these Fourier samples are often termed as navigators or training data. The navigators can either be estimated by a short training scan before the actual acquisition, or be interleaved with the actual acquisition (see Fig.(3)). If γ is periodic in time (e.g. cine imaging), the frequencies can be assumed to be multiples of the fundamental frequency (cardiac rate). If the temporal frequencies are known apriori, the coefficients $u_i(\mathbf{r})$ can be determined even from under-sampled $k - t$ measurements.

In a second step, u_i is determined in a least square sense by fitting the acquired $k - t$ data ($\mathbf{b}$) to the model in Eq.(5):

$$\min_{u_i(\mathbf{r})} \left\| \mathcal{A} \left(\sum_{i=1}^{R} u_i(\mathbf{r}) e^{j2\pi f_i t} \right) - \mathbf{b} \right\|_2^2; \qquad (6)$$

The above idea was made rigorous by in a series of developments by Bressler et.al [15–19], who reformulated the problem as the design of a lattice sampling pattern to minimize aliasing. Once a sampling scheme that does not result in aliasing is identified, Eq.(6) reduces to a simple Fourier domain filtering problem. This approach is related to spatial-spectral support constrained reconstruction schemes such as UNFOLD [20, 21], and k-t BLAST [22]. All of these methods design of specialized coherent $k - t$ sampling patterns such that there are few signal overlaps (aliases) in the spatial-spectral space or popularly known as the $x - f$ space. (also see Fig.(3)).

While the above methods are powerful, the periodic nature of the model and the assumption of stationarity restricts its use in many DMRI applications with complex spatio-temporal patterns. For example, any deviations in cardiac rate/breath-holding location between the training and the actual acquisitions will result in model mis-match and hence compromised performance. In addition, it requires specialized sequences with appropriate navigators and ability to change the sampling patterns on the fly depending on the cardiac rate. To address this, several researchers have instead proposed to acquire the data using incoherent sampling pattens and use compressed sensing assuming Fourier dictionaries.

0.4.2   Compressed sensing

Compressed sensing (CS) methods have shown promise to accelerate DMRI [23–28]. CS under the synthesis basis representation can be viewed as modifying

the DMRI global model as:

$$\gamma(\mathbf{x}, t) = \sum_{i=1}^{R} \underbrace{u_i(\mathbf{r})}_{\text{sparse}} \underbrace{v_i(t)}_{\text{Pre}-\text{determined dictionary}} ; R \geq N; \tag{7}$$

where the choice of basis functions are determined a-priori. Unlike linear models, these basis functions $v_i(t)$ can belong to a set of basis or an over-complete dictionary (e.g. wavelet frames). For example, in applications with quasi-periodic spatio-temporal dynamics (e.g. breath held cardiac cine imaging), the dictionary can be chosen as exponentials with all possible temporal frequency components:

$$\gamma(\mathbf{r}, t) = \sum_{i=1}^{R} \underbrace{u_i(\mathbf{r})}_{\text{sparse}} e^{j2\pi f_i t}; R > N, \tag{8}$$

where R is the size of the Fourier dictionary.

CS assumes that the model coefficients $u_i(\mathbf{r})$ are assumed to be sparse and estimate them from the measured $k-t$ space data by solving the ℓ_1 optimization scheme:

$$\{u_i(\mathbf{r})\} = \arg \min_{u_i(\mathbf{r})} \|\mathcal{A}(\gamma) - \mathbf{b}\|_2^2 + \lambda \sum_{i=1}^{R} \|u_i(\mathbf{r})\|_1. \tag{9}$$

Here, γ is specified by Eq.(8) and the ℓ_1 norm of the coefficient image $u_i(\mathbf{r})$ is the sum of absolute values of the pixels:

$$\|u_i(\mathbf{r})\|_1 = \sum_{\mathbf{r}} |u_i(\mathbf{r})|. \tag{10}$$

Here, λ is a regularizing parameter that controls the trade-off between data consistency and the sparsity constraint. The advantage of CS over spatial-spectral support based methods (linear models) is that it does not require training data to estimate the support. It uses incoherent $k-t$ sampling that results in incoherent alias artifacts. The solution of Eq.(9) will provide sparse coefficients, which implies that only the basis functions $v_i(t)$ corresponding to the non-zero coefficients $u_i(\mathbf{r})$ are active at each voxel. In other words, unlike the two step linear models, CS jointly estimates the exponential basis functions, and the associated model coefficients. In addition, the set of exponentials that are active at different voxels could be different. For example, one set of exponentials would be active on the cardiac regions where the motion is at the cardiac rate, while another set of exponentials could be chosen on the liver regions where the motion patterns are different.

An alternative to synthesis formulation specified by Eq.(9) is to use an analysis formulation:

$$\gamma(\mathbf{r}, t) = \arg \min_{\gamma} \|\mathcal{A}(\gamma) - \mathbf{b}\|_2^2 + \lambda \|\psi(\gamma)\|_1; \tag{11}$$

where ψ is an appropriate sparsity inducing operator. For example, ψ can be chosen as the Fourier transform [23,26], spatio-temporal wavelet [29], or spatio-temporal finite difference operator [30].

The CS approach eliminates the need for training scans and customized $k-t$ sampling as required by linear models, described in the earlier subsection. However, the performance of CS is heavily dependent on the specific dictionary or sparsifying operator. For example, Fourier dictionaries may be ideally suited for breath-held cine applications due to the pseudo-periodicity of cardiac motion. However, the motion/contrast variations are not periodic in several other applications; the use of Fourier dictionaries may be sub-optimal in these applications. Specifically, many transform coefficients are required to accurately represent complex spatio-temporal patterns in applications such as free breathing cardiac perfusion MRI (see how the motion and contrast dynamics disturbs the $x - f$ sparse representation in Fig.(5)). This limits the maximum achievable acceleration rate, which prompted researchers to investigate data adaptive representations which are discussed in the next sections.

0.5 Blind models for dynamic MRI

In this section, we will describe adaptive models that learns the representation from the data itself. Since the representation is learned and not pre-determined as the linear and compressed sensing models used in the previous sections, we term them as blind models.

0.5.1 Blind linear models

Blind linear models can be thought of as a generalization of the adaptive linear model (DIME) to non-periodic dynamic datasets; instead of assuming the temporal basis functions to be periodic exponentials, they are assumed to be arbitrary functions. The representation of the signal as a linear combination of a few arbitrary basis functions implies considerable correlations between the temporal profiles of the dataset. Liang et. al., proposed to re-arrange the spatio-temporal signal $\gamma(\mathbf{r}, t)$ in a Casorati matrix form to exploit the correlations within the data [13]:

$$\mathbf{\Gamma} = \begin{bmatrix} \gamma(\mathbf{r}_1, t_1) & \dots & \gamma(\mathbf{r}_1, t_N) \\ \vdots & & \\ \gamma(\mathbf{r}_M, t_1) & \dots & \gamma(\mathbf{r}_M, t_N) \end{bmatrix} \tag{12}$$

The rows of $\mathbf{\Gamma}$ correspond to the voxels, while the columns represent the temporal samples. The rows of this $M \times N$ matrix are often linearly dependent (also see Fig.(4)). Hence, the rank of $\mathbf{\Gamma}$, is given by $R << \min(M, N)$. An arbitrary $M \times N$ matrix of rank R can be decomposed as

$$\mathbf{\Gamma} = \underbrace{\mathbf{U}}_{M \times R} \underbrace{\mathbf{\Sigma}}_{R \times R} \underbrace{\mathbf{V}^H}_{R \times N}. \tag{13}$$
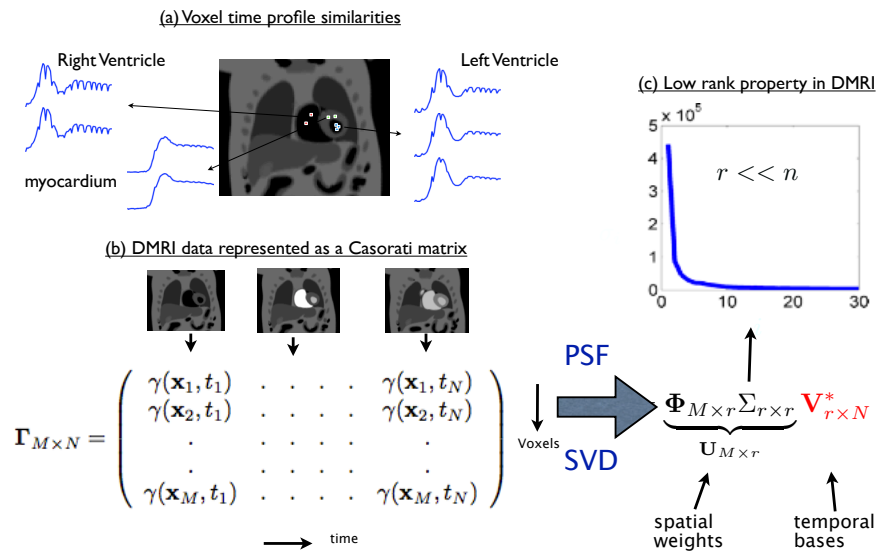
9

Figure 4: Low rank structure in DMRI data: The blind linear models exploit similarities amongst the voxel time profiles in DMRI data, as depicted in the numerical phantom example of a cardiac perfusion MRI dataset in (a). As shown in (b), the data can be rearranged as a Casorati matrix, by row/or column wise stacking of voxels from every time frame of the DMRI series. A PCA/SVD/KLT of the resultant matrix reveals the low rank structure of the data, where the singular values of the dataset exhibit a rapid decay (c).
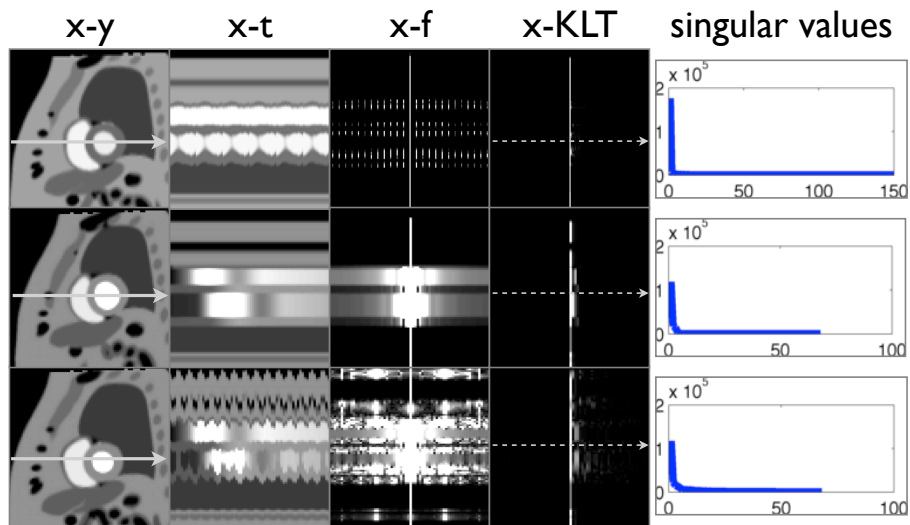
Figure 5: Data representation in different transform domains: A numerical cardiac phantom is considered to mimic breath held cine data in the top row, breath held perfusion data in the middle row, and free breathing perfusion data in the bottom row. The first column shows the spatial image (x-y) for a specific time frame; the second column depicts the image time profile (x-t) through the arrows in the first column. The x-f and x-KLT representations are shown in the third and fourth columns. The significant singular values in the KLT model are shown in the fifth column. Note that the x-f space is highly sparse for breathheld cine applications, while the sparsity is disturbed significantly in perfusion and breathing applications. In contrast, as seen in the fourth and fifth columns, all the datasets are compact in their x-KLT spaces.

This decomposition implies that the spatio-temporal signal $\gamma(\mathbf{r}, t)$ can be partially separable upto R^{th} order as [13, 31–33]:

$$\gamma(\mathbf{r}, t) = \sum_{i=0}^{R-1} u_i(\mathbf{r}) \underbrace{v_i(t)}_{\text{from PCA/KLT/SVD}} ; \tag{14}$$

The temporal basis functions $v_i(t)$ are the columns of the matrix $\mathbf{V}$ in Eq.(13), while the spatial weights $u_i(\mathbf{r})$ are the row vectors of $\mathbf{U\Sigma}$ (often termed as spatial weights). Since the basis functions are derived from the data itself, these models can be termed as blind linear models. The data-driven capabilities of this model offers a much more compact representation in comparison to the linear models that use spectral basis functions; the representation of this model in different DMRI applications is illustrated in Fig.(5).

The methods of partially separable functions (PSF), k-t PCA, k-t FOCUSS proposed the following two-step strategy to reconstruct the spatio-temporal signal [13, 23, 31–33].

1. Estimate the temporal basis functions $v_i(t)$; $i = 0, .., R-1$ using PCA/KLT/SVD of the training image time-series. The training data consists of dynamic image data, acquired with low-spatial resolution and high temporal sampling rate; it is obtained as the IFFT of the central phase encodes, acquired at the Nyquist temporal sampling rate.

2. Use the linear model specified by Eq.(14) to recover the DMRI data from sub-Nyquist sampled measurements, using the temporal basis functions $v_i(t)$. This involves the estimation of the spatial weight images $u_i(\mathbf{x})$; $i = 0, .., r-1$ from the under-sampled measurements in a least squares sense:

$$\min_{u_i(\mathbf{r})} \left\| \mathcal{A} \left(\sum_{i=1}^{R} u_i(\mathbf{r}) \underbrace{v_i(t)}_{\text{from PCA/KLT/SVD}} \right) - \mathbf{b} \right\|_2^2 ; \tag{15}$$

Since $R << N$, this approach provides a significant reduction in the number of unknowns and hence the number of measurements.

The blind linear models (BLM) implicitly assume that the principal basis functions estimated from the low-resolution data closely approximate the actual PCA/SVD/KLT basis functions. We have derived theoretical conditions for the equivalence of the right subspace estimated from the navigator data to the one estimated from the full data [34]. The results show that the equivalence can break down when the number of phase encodes in the training data are too few, resulting in the loss of subtle details and reconstructions with inaccurate temporal dynamics. While the acquisition of more training data can minimize these problems, this comes at the expense of the number of high-frequency encodes that can be acquired at a specified acceleration rate; this can often result in aliasing artifacts [35]. Sufficient conditions for the subspace aware recovery
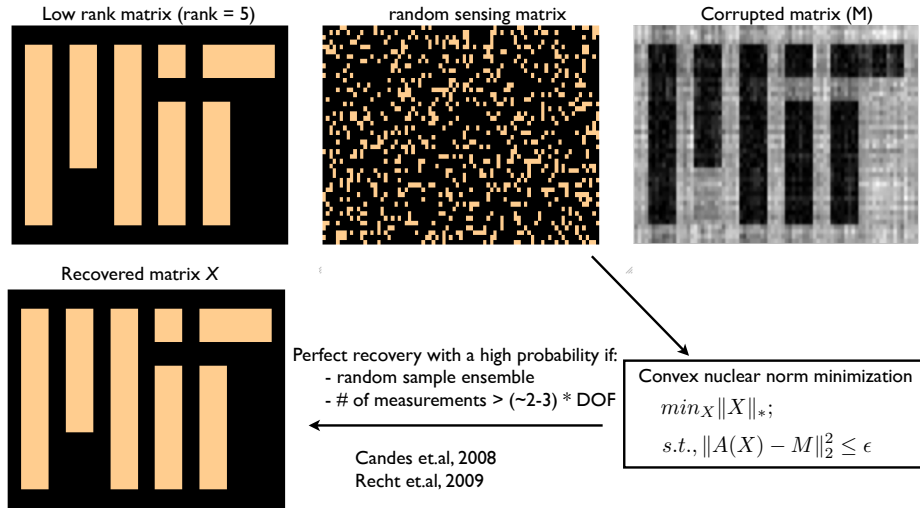
12

Figure 6: Recovery of a low rank matrix from incoherently under sampled measurements can be posed as a convex rank minimization problem: Recent theoretical results [36] [37] indicate the matrix can be perfectly recovered with a high probability if (a) random ensemble measurement matrix is employed, and (b) if the number of measurements are approximately two to three times the degrees of freedom of the low rank matrix. Here $\|\|_*$ indicates the nuclear norm of the matrix, defined as the sum of singular values of the matrix.

of the signal γ (recover of $u_i; i = 1, .., R$) from under sampled measurements are also available [34]; the theoretical results enable the determination of appropriate sampling patterns for each application (e.g. cine and perfusion MRI). The bottom line is that the performance of the two-step schemes requires a fine balance between the amount of training data and the number of high-frequency encodes. Single step low-rank recovery provides an alternate approach that will minimize these tradeoffs.

0.5.2 Low rank matrix recovery

The blind linear models described previously assumes the dynamic data to lie in a low dimensional sub-space. This assumption leads to the Casorati matrix $\boldsymbol{\Gamma}$ being low rank (also see Fig.(4)). The recovery of a low-rank matrix from few of its incoherent measurements has been studied extensively in the fields of applied mathematics and signal processing. The recent theoretical results indicate that a matrix $\boldsymbol{\Gamma} \in \mathbb{R}^{m \times n}$ of rank $R; R \leq \min(M, N)$ can be perfectly recovered from its measurements $\mathbf{b} = \mathcal{A}(\boldsymbol{\Gamma})$ by solving the constrained optimization problem [36, 37] (also see Fig.(6)):

$$\boldsymbol{\Gamma}^* = \arg \min_{\boldsymbol{\Gamma}} \|\mathcal{A}(\boldsymbol{\Gamma}) - \mathbf{b}\|^2 \text{ such that } \text{rank}(\boldsymbol{\Gamma}) \leq R. \tag{16}$$
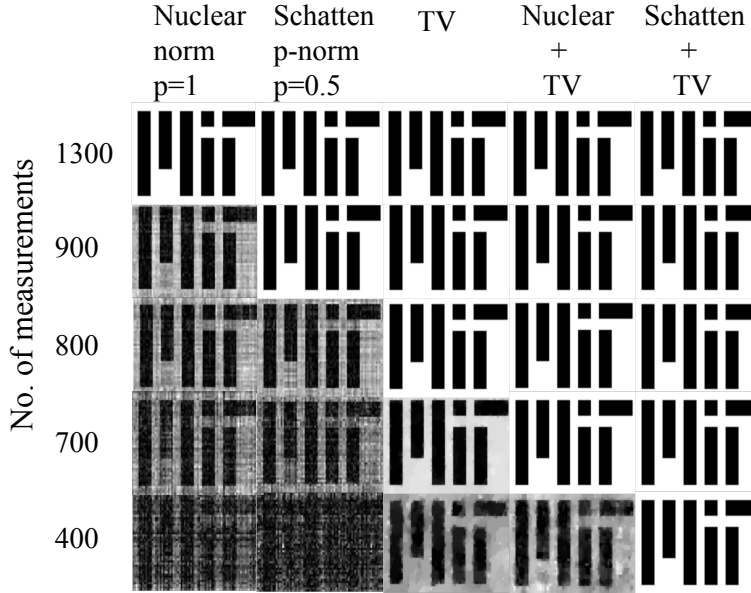
Figure 7: Demonstration of recovery rates using different norms: The matrix with the MIT logo has a low rank structure (rank of five), as well as a sparse structure (sparse gradients of the rows and columns). This matrix is recovered from different random ensemble measurement matrices, which correspond to different rates of under sampling. The combined use of low rank and sparse priors yield better recovery rates over using the low rank or the sparse prior individually. In addition, the performance of the low rank prior can be improved by using the non-Convex Schatten p-norm ($p = 0.5$) over the convex nuclear norm ($p = 1$).

The above formulation can be applied to recovering DMRI data from undersampled $k - t$ measurements subject to the constraint that $\mathbf{\Gamma}$ is low rank. Reformulating the above constrained optimization problem using Lagrange's multipliers, one can obtain:

$$\mathbf{\Gamma}^* = \arg\min_{\mathbf{\Gamma}} \|\mathcal{A}(\mathbf{\Gamma}) - \mathbf{b}\|^2 + \lambda \operatorname{rank}(\mathbf{\Gamma}). \qquad (17)$$

Since the rank penalty is non-convex, it is often replaced with the nuclear norm, which is the closest convex relaxation. The nuclear norm of an R-rank matrix $\mathbf{\Gamma} = \mathbf{U\Sigma V}^*$, denoted by $\|\mathbf{\Gamma}\|_*$, is the sum of the singular values of $\mathbf{\Gamma}$ ($\|\mathbf{\Gamma}\|_* = \sum_i (\mathbf{\Sigma}_{i,i})$). With this relaxation, the recovery of the matrix is simplified as [37]:

$$\mathbf{\Gamma}^* = \arg\min_{\mathbf{\Gamma}} \|\mathcal{A}(\mathbf{\Gamma}) - \mathbf{b}\|^2 + \lambda \|\mathbf{\Gamma}\|_*; \qquad (18)$$

The above optimization has benefits over blind linear models in that it jointly estimates the spatial weights and the temporal basis functions, there by address-

14

ing the practical limitation of the tradeoffs amongst sampling in the training and data acquisition phases.

Matrix recovery schemes using non-convex optimization have also been proposed which demonstrate improved recovery rates over nuclear norm minimization. One approach is the replacement of the convex nuclear norm in Eq.(18) by the non-convex on-convex Schatten p-norm ($p < 1$) [35]:

$$\mathbf{\Gamma}^* = \arg \min_{\mathbf{\Gamma}} \|\mathcal{A}\left(\mathbf{\Gamma}\right) - \mathbf{b}\|^2 + \lambda \underbrace{\left(\sum_{i=1}^{\min(M,N)} (\mathbf{\Sigma}_{i,i})^p \right)}_{\text{Schatten p norm}}; 0 < p < 1 \qquad (19)$$

A greedy incremented rank power factorization (IRPF) approach has also been proposed [38, 39], which iterates between solving for the model coefficient matrix $\mathbf{\Phi}_{M \times R} = \mathbf{U}_{M \times R} \mathbf{\Sigma}_{R \times R}$ and the temporal basis functions matrix $\mathbf{V}_{R \times N}$:

$$\min_{\Phi_{M \times R}} \|\mathcal{A}(\mathbf{\Phi}\mathbf{V}) - \mathbf{b}\|_2^2; \qquad (20)$$

$$\min_{\mathbf{V}_{R \times N}} \|\mathcal{A}(\mathbf{\Phi}\mathbf{V}) - \mathbf{b}\|_2^2; \qquad (21)$$

The optimization with these non-convex methods differ from the nuclear norm minimization schemes; they rely heavily on using continuation strategies to avoid convergence to undesirable local minima. For example, the IRPF algorithm iterates between Eq.(20), and Eq.(21) by starting with a rank $R = 1$, and gradually increment the rank in steps of one, until the desired rank, $R < N$ is achieved. In other words, they solve for simpler subproblems during the initial iterations, and gradually update the complexity of the problem as the iterations proceed. We refer the interested reader to [38] [40] for details of these algorithms.

The low rank and the two-step $PSF/k - t$ PCA methods assume the data to be globally low-rank, which implies that the voxel profiles at all voxels have the same representation. Since the voxel profiles of different anatomical regions may be distinct (e.g. motion patterns of the heart and the lung may be very different), the above model may be too restrictive. Specifically, a high model order (high rank) may be needed to represent all regions accurately. Region based priors in DMRI have been recently explored by several researchers [41–46]. In contrast to global models, these schemes utilize different model representation for different localized regions of the spatio-temporal object. The locally low rank model exploits rank deficiency of small spatial patches in the DMRI time series as opposed to considering rank deficiency of the whole Casorati matrix as done the blind linear model. Rank deficiency of matrices formed from voxel time profiles belonging to anatomically distinct regions have been proposed in the method of compartment based $k - t$ PCA [43]. This scheme segments regional compartments such as left ventricle, myocardium, and right ventricle in myocardial perfusion MRI, and promotes rank-deficiency independently to each

of these compartments. [46] further improved this approach by considering rank deficiencies on elements which are not only spatially localized, but also temporally localized; which was motivated by temporal dynamics in contrast enhanced MRI, where image frames during initial contrast passage varies significantly in contrast from the later frames.

0.5.3 Joint Low rank and Sparsity regularized recovery (k-t SLR)

The performance of low rank constrained DMRI methods can be further improved by utilizing additional sparsity based priors (also see Fig.(7), where the performance recovery a matrix which is perfectly low rank and sparse is demonstrated with different priors). For instance, the method of $k - t$ SLR utilizes a spatio-temporal total variation prior in addition to the Schatten p-norm low rank prior as [35]:

$$\mathbf{\Gamma}^* = \arg \min_{\mathbf{\Gamma}} \|\mathcal{A}(\mathbf{\Gamma}) - \mathbf{b}\|^2 + \lambda_1 \underbrace{\left(\sum_{i=1}^{min(M,N)} (\mathbf{\Sigma}_{i,i})^p \right)}_{\text{Schatten p norm}} + \lambda_2 \underbrace{\left\| \sqrt{|\nabla_x(\mathbf{\Gamma})|^2 + |\nabla_y(\mathbf{\Gamma})|^2 + \alpha|\nabla_t(\mathbf{\Gamma})|^2} \right\|_1}_{\text{spatio-temporal total variation}};$$

(22)

where $\lambda_1, \lambda_2, \alpha$ are regularization parameters.

$k - t$ SLR utilizes variable splitting techniques to decouple the above problem to simpler subproblems of (a) singular value shrinkage, (b) sparsity shrinkage, (c) quadratic reconstruction. It iterates between these problems using a continuation strategy to avoid convergence to local minima. Other extensions such as alternating direction method of multiplies, and Bregman multipliers have been proposed. We refer the reader to [47, 48] for details of these algorithms. Fig.(8) demonstrates the image quality with $k - t$ SLR in comparison with CS that utilize temporal Fourier basis on a free breathing myocardial perfusion dataset with shallow breathing. As seen in this figure, $k - t$ SLR is shown to provide superior depiction of subtle perfusion defects, and is more robust to motion artifacts due to the use of data-driven basis, and complementary benefits provided by the sparsity priors.

The two step recovery scheme of the blind linear model has also been improved by utilizing additional sparsity constraints [49]. These improve the recovery of the $u_i(\mathbf{r})$ problem in Eq.(15) as:

$$u_i^*(\mathbf{r}) = \arg \min_{u_i(\mathbf{r})} \left\| \mathcal{A} \left(\sum_{i=1}^{R} u_i(\mathbf{r}) \underbrace{v_i(t)}_{\text{from PCA/KLT/SVD}} \right) - \mathbf{b} \right\|_2^2 + \lambda \underbrace{\left\| \psi \left(\sum_{i=1}^{R} u_i(\mathbf{r}) v_i(t) \right) \right\|_1}_{\text{sparsity penalty}};$$

(23)

where the choice of ψ in Eq.(23) is motivated by the DMRI application. For instance, in dynamic imaging of speech production, the optimization in Eq.(23)
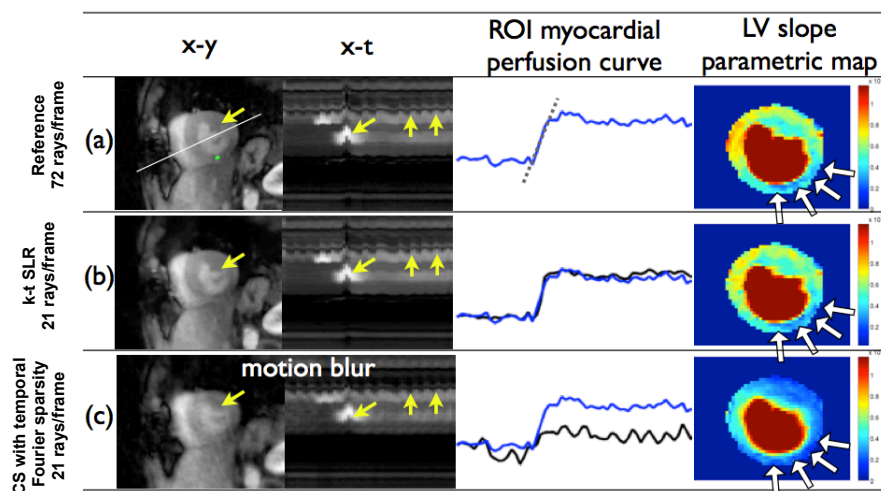
Figure 8: Comparison of $k-t$ SLR with CS with $x-f$ sparsity on a dataset of a patient with myocardial ischemia. The first row corresponds to the close to fully sampled reference data with 72 radial rays per frame. Retrospective sampling of choosing 21 radial rays/frame from the acquired data was considered. These rays were chosen such that the spacing between successive rays approximated the golden ratio. The $x-y$, $x-t$, region of interest (marked by green in the top left image) myocardial perfusion curve and the left ventricle parametric map of the slopes of the perfusion curves are shown in the column. In the perfusion maps in (a), regions of reduced perfusion uptake are depicted in the inferior myocardium wall (as pointed by the white arrows). It is observed that the $k-t$ SLR reconstructions depict these regions efficiently in comparison to CS methods (see (b),(c)); the latter in particular is sensitive to motion and results in motion blur artifacts; this is depicted in the reconstructions as well (see the yellow arrows).

(a) CS exploiting Fourier sparsity   (b) Dictionary unaware: Blind CS   (c) Dictionary aware
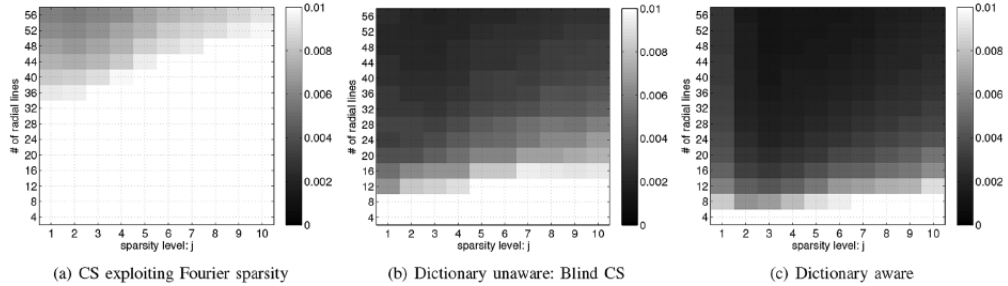
Figure 9: Phase transition recovery rate experiment: Ground truth DMRI datasets were created with different sparsity levels under known dictionaries. The datasets were under sampled using different $k - t$ radial measurement matrices. The performance recovery of three algorithms were studied by plotting the root mean square error of the reconstructions at different sparsity levels: (a) CS with $v_i(t)$ to be exponential basis functions, (b) Blind CS with unknown $v_i(t)$, but estimated from the under sampled data (i.e, solving Eq. 25), (c) Dictionary aware setting (i.e, CS with the ground truth known). As expected, the number of measurements required to recover the datasets increases with the sparsity level. The BCS scheme outperforms the CS scheme considerably. Furthermore, due to a small over head in estimating the dictionary, the dictionary unaware scheme (BCS) was only marginally worse than the dictionary aware scheme.

with ψ being the temporal Fourier transform demonstrated excellent acceleration capabilities translating to prospective acquisition of dynamic speech images at 100 frames per second [50].

0.5.4 Blind Compressed Sensing

The blind compressed sensing (BCS) model [51] share similarities with CS and blind linear models. Similar to CS, the voxel intensity profiles are modeled as a sparse linear combination of basis functions in a dictionary. However, instead of assuming a fixed dictionary, BCS estimates the dictionary from the undersampled measurements itself, leading it to offer a data-driven representation. BCS contrasts with blind linear models in terms of the sparsity assumption on the coefficients, and the increased number of basis functions in the dictionary (which are not necessarily orthogonal); which together provides a richer representation. The global signal model for BCS can therefore be expressed as:

$$\gamma(\mathbf{x}, t) = \sum_{i=1}^{R} \underbrace{u_i(\mathbf{r})}_{\text{Sparse coefficients}} \underbrace{v_i(t)}_{\text{Learned basis}} \quad ; R \geq N; \qquad (24)$$

The differences of BCS and blind linear models can also be highlighted by investigating the degrees of freedom in these models. The number of degrees

18

of freedom (DOF) of the general global model approximates to $MR + RN$. In blind linear models, since $R << N$, the DOF is approximately MR, or proportional to the rank R. In the BCS model, the DOF is approximately $MK + RN$, where K is the average sparsity of the representation. However, in DMRI, since $M >> N$ the DOF is dominated by the average sparsity k and not the dictionary size R, it reduces to MK. In other words, the DOF in BCS is proportional to the average sparsity level K, or the average number of basis functions active at a voxel, which in DMRI is often less than the rank R in a blind linear model representation. This implies that the BCS model is capable to provide an improved trade-off between accuracy and achievable acceleration in comparison to the blind linear model.

The main utility of using BCS over CS is that basis functions in BCS are more representative of the temporal dynamics at hand and adapt to the data; they provide sparser representation compared to off the shelf dictionary bases (eg: Fourier exponential bases) as used in CS. Further in DMRI since the number of voxels per frame typically dominate the number of time frames, the overhead in learning the basis functions is minimal. This is demonstrated in the example phase transition plot in Fig.(9) of CS with temporal Fourier bases v/s BCS with learned bases from undersampled data v/s a setting where the ideal dictionary bases are known. Since the coefficients $u_i(\mathbf{r})$ are sparse, the basis functions that are active at each voxel are different. Thus, this approach can be thought of as a locally low-rank scheme, where the representation is allowed to vary depending on the pixel.

The reconstruction in BCS involves the joint estimation of $u_i(\mathbf{r})$, and $v_i(t)$ in Eq.(24) from under sampled $k - t$ measurements ($\mathbf{b}$) with a sparsity constraint on $u_i(\mathbf{r})$, and a dictionary constraint on $v_i(t)$, which is required to avoid scale ambiguity in the product of $u_i(\mathbf{x})v_i(t)$. Choices of sparsity and dictionary constraints can range from utilizing the convex l_1 norm, or the non-convex l_0, l_p; $(0 < p < 1)$ norms on $u_i(\mathbf{x})$, and unit column norm or Frobenius norm constraints on the dictionary. A typical BCS reconstruction with l_1 coefficient sparsity, and unit column norm dictionary constraint can be formulated as the following constrained optimization problem:

$$
\{u_i(\mathbf{r}), v_i(t)\} \quad = \quad \arg \min_{u_i(\mathbf{r}), v_i(t)} \left\| \mathcal{A} \left(\sum_{i=1}^{R} u_i(\mathbf{r}) v_i(t) \right) - \mathbf{b} \right\|_2^2 + \lambda \left\| u_i(\mathbf{r}) \right\|_1 ;
$$
$$
\text{such that } \|v_i(t)\|_2^2 < 1; \; i = 1, .., R \tag{25}
$$

A straightforward optimization algorithm to solve Eq.(25) involves alternating between updating $u_i(\mathbf{x})$, and $v_i(t)$. Faster approaches that involve continuation strategies have also been proposed [51].

Fig.(10) shows a comparison of under sampled reconstruction with the low rank model using Schatten p-norm regularization; $p < 1$), the CS model with temporal Fourier sparsity, and the BCS model. As depicted in this figure, the BCS model can offer better temporal fidelity, in particular the richer data-driven
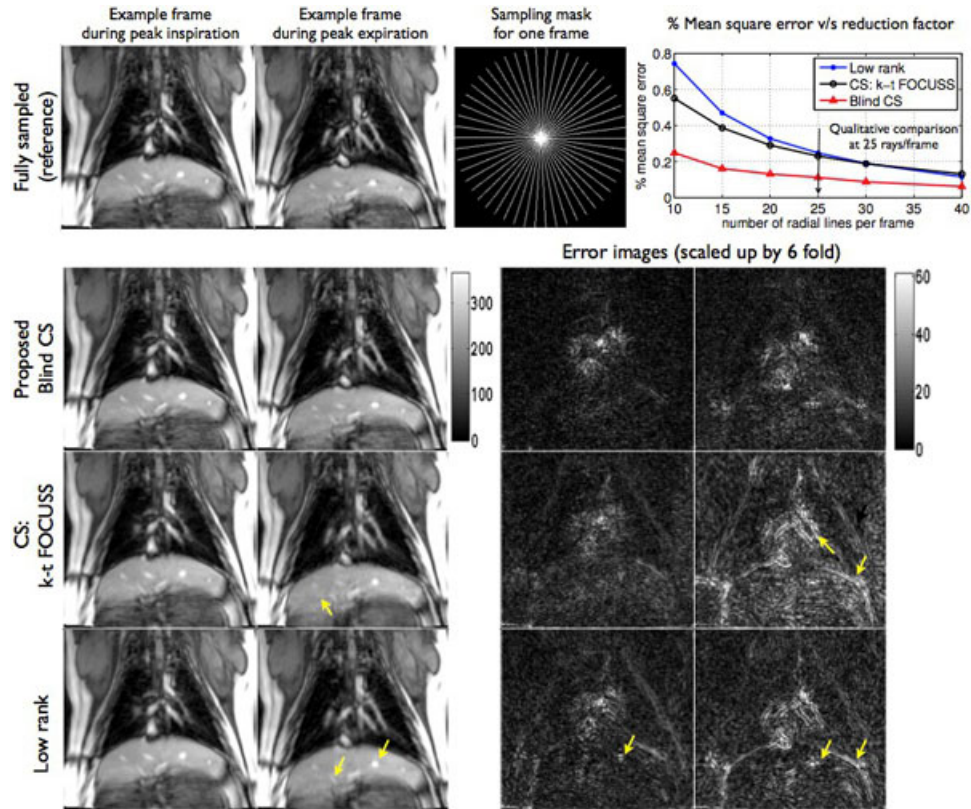
Figure 10: Performance evaluation of undersampled reconstruction of a dynamic lung MRI dataset using the blind compressed sensing (BCS), CS and low rank schemes: It can be seen that the BCS scheme consistently produce the least mean square error at all undersampling factors. The CS, and low rank schemes depict loss in spatial features, and compromises due to motion blurring (see the yellow arrows in rows 3,4). In contrast, the BCS scheme was found to be more robust to motion blur, and provided superior spatio-temporal fidelity.

basis adapts to learning the spatio-temporal dynamics much efficiently than the blind linear model, and the CS models.

Other flavors of BCS with dictionaries containing atoms of three-dimensional spatio-temporal cubes [52, 53] have been proposed. These schemes have shown considerable promise over conventional CS schemes in the cardiac cine MRI application.

0.6 Deformation compensated compressed sensing

All of the above methods model the voxel profiles in the dynamic dataset as a linear combination of basis functions. The performance of all of these schemes degrade with extensive motion in the datasets, which are present in free breathing and ungated acquisitions. Specifically, different anatomical regions may pass through each voxel due to respiratory/cardiac motion; a high model order is needed to represent the signal at hand, which results in lower acceleration. Methods based on compensating the inter-frame object and/or subject motion have been used in several DMRI reconstruction methods [54–57]. For instance, the k-t FOCUSS with motion estimation and compensation (ME/MC) [55] method models the dynamic images as the deformation of fully sampled reference frames. The residuals are then reconstructed from under-sampled k-space data using $k-t$ FOCUSS.

An explicit motion compensated recovery scheme, which jointly estimates the deformation parameters and the motion compensated dataset was introduced [57, 58]. The main advantage of this scheme is its ability to impose arbitrary compactness priors on the motion compensated dataset (e.g sparsity, low-rankedness), thus making it applicable in a range of applications including ungated free breathing myocardial perfusion MRI and free breathing CINE. This deformation compensated compressed sensing (DC-CS) scheme, jointly estimates the deformation and dynamic images subject to arbitrary compactness priors on the deformation corrected dynamic dataset:

$$\min_{\gamma(\mathbf{r},t),\theta(\mathbf{r},t)} \|\mathcal{A}(\gamma) - \mathbf{b}\|_2^2 \quad + \lambda \quad \underbrace{\Phi\left(\mathcal{T}_\theta \cdot \gamma\right)}_{\text{compactness prior}} . \quad (26)$$

Here, $\mathcal{T}_\theta$ denotes the deformation operator, parametrized by θ. The motion field can be modeled as rigid body motion or smooth deformations. Φ specifies arbitrary choices of compactness priors, such as the spatial-spectral sparsity prior $\Phi(u) = \|\mathcal{F}_t\|_{\ell_1}$, or the the temporal finite difference sparsity prior $\Phi(u) = \|\nabla_t\|_{\ell_1}$. $\mathcal{F}_t$ and ∇_t are the temporal Fourier transform and temporal gradient operator, respectively. Low rank priors can be defined as $\Phi(\gamma) = \|\mathbf{\Gamma}\|_*$, the nuclear norm of the Casorati matrix $\mathbf{\Gamma}$ associated with $\gamma(\mathbf{x}, t)$ [13, 35]. The presence of a global cost function enables the use of continuation strategies to minimize local minima effects.

The optimization in Eq. (11) is solved using a variable splitting optimization framework, where the problem is reduced to iterations between simpler problems of shrinkage based denoising, deformable registration, and quadratic optimization. The shrinkage based denoising subproblem results in a reference time image series containing only dynamics due to contrast changes without the motion. The specific form of the reference image time series enables the scheme to decouple the effects of smooth perfusion induced contrast changes and the more rapid changes resulting from inter-frame motion, which makes this approach applicable to dynamic contrast enhanced MRI applications while using simpler similarity measure metrics for registration. Fig.(11) demonstrates the application of the DC-CS scheme using the spatial-spectral sparsity prior and the temporal total variation prior in reconstruction a free breathing myocardial perfusion MRI dataset from approximately seven fold under sampled measurements.

The DC-CS approach has similarities to recent motion compensated schemes such as motion adaptive spatio-temporal regularization (MASTER) [59]. This scheme focusses on breath-held cardiac cine applications and alternates between the estimation of cardiac motion by using an optical flow or phase based motion estimation and reconstruction using total variation priors on the motion compensated dataset. Other motion compensated schemes customized to free breathing cardiac cine and delayed enhancement MRI have also been introduced [54, 60–63]. In applications involving changes in contrast along time (eg. perfusion MRI, and parametric MRI), customized ME/MC schemes that model the contrast variations using a parametric perfusion model have been developed. These schemes derive a dynamic reference image time series which contain only perfusion dynamics in the absence of motion [64], and [65]. The deformation due to motion was modeled using a rigid transformation model in [64], and a more accurate non-rigid model in [65]. Some approaches rely on the use of mutual information similarity measure during registration which is robust to the presence of contrast changes [56]. The scheme in [56] jointly estimates the deformation (using a mutual information similarity measure), and the dynamic images, while enforcing regional rank sparsity on the dynamic images.

0.7   Dynamic MRI using manifold models

The manifold structure of data has been widely used for the visualization of the structure of complex datasets. Non-linear dimensionality reduction or manifold embedding methods assume that the data are points on a low dimensional manifold (smooth surface) in higher dimensional space. If the manifold is of low-enough dimensionality, the data can be compactly visualized in low-dimensional space. For example, if the points are on a curve in 3-D, one can associate each point to a point on a straight line; non-linear dimensionality reduction methods such as ISO-MAP generates a nonlinear mapping between each point on the 3-D curve to a point on a line [66–68]. Emerging research shows that the manifold structure of dynamic MRI data can be used to regularize the recovery of static
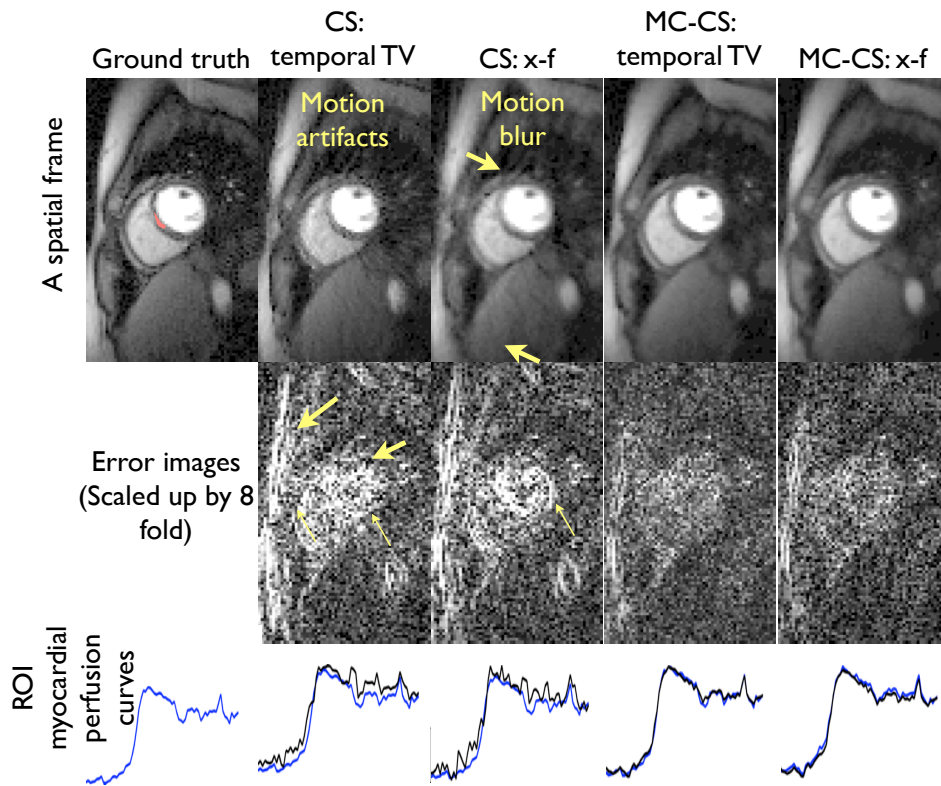
Figure 11: Recovery of a free breathing myocardial perfusion MRI data set from seven fold under sampled data using the deformation corrected compressed sensing algorithm. The joint estimation of the inter-frame motion along with the reconstruction greatly improves the fidelity to motion artifacts. Note the motion blurring and artifacts in CS reconstructions, in comparison to the motion compensated CS reconstructions (see arrows).

and dynamic MRI data from under sampled measurements.

0.7.1 Image manifold regularization: application to real time cardiac MRI

Emerging research shows that the manifold structure of dynamic MRI data can be used to regularize the recovery from under sampled data. In many applications (e.g. free breathing and ungated CINE), the images in the dataset can be assumed to non-linear functions of two parameters: the cardiac phase and respiratory phase. Images with similar cardiac and respiratory phase are expected to be similar; this property is used in gating methods. Hence, the images in these applications can be safely assumed to be points on a smooth low-dimensional manifold with high ambient dimension (the ambient dimension is the total number of pixels in each image).

The manifold structure of dynamic MRI data has been used by Usman et al, who estimated cardiac and respiratory gating signals from free breathing and ungated cine MRI data using manifold embedding. Specifically, they perform a preliminary high temporal resolution recovery of the golden angle radial acquisition using iterative SENSE. By performing a localized manifold learning strategy on regions around the heart, they obtain the cardiac gating signal. Once the cardiac gating signal is obtained, they bin the data from the sysolic phases and perform a low temporal resolution reconstruction, followed by manifold learning to identify the respiratory signal. Once both gating signals are obtained, they data from similar cardiac gates are binned together to perform the final k-t sparse SENSE reconstruction.

An alternate manifold regularization strategy that relies on a navigated golden angle radial acquisition was introduced in [69, 70] for the reconstruction of free breathing and ungated cine MRI data. The acquisition scheme collects a few (2-4) radial k-space navigator k-space lines from each frame γ_i, while the remaining lines are acquired according to the classical golden angle radial scheme:

$$\underbrace{\begin{bmatrix} \mathbf{y}_i \\ \mathbf{z}_i \end{bmatrix}}_{\mathbf{b}_i} = \underbrace{\begin{bmatrix} \mathbf{\Phi} \\ \mathbf{B}_i \end{bmatrix}}_{\mathbf{A}_i} \gamma_i \tag{27}$$

Here, $\mathbf{\Phi}$ denotes the Fourier sampling operator corresponding to the navigator lines, while $\mathbf{B}_i$ are the measurements corresponding to the remaining lines. The recovery of the image frames is posed as the discretized Tikhonov regularized reconstruction on the manifold:

$$\{\gamma_i^*\} = \arg \min_{\gamma_i} \sum_{i=1}^{k} \|\mathbf{A}_i \, \gamma_i - \mathbf{b}_i\|_F^2 + \lambda \operatorname{Tr}(\mathbf{\Gamma} \, \mathbf{L} \, \mathbf{\Gamma}^H) \tag{28}$$

where $\mathbf{\Gamma} = \begin{bmatrix} \gamma_1 & \gamma_2 & \dots & \gamma_k \end{bmatrix}$ and Tr denotes the trace operator. Here, $\mathbf{L}$ is the discretization of the Laplacian operator of the manifold. The matrix $\mathbf{L}$ is

estimated from the common measurements $\mathbf{y}_i$ as

$$\mathbf{L}_{i,j} = \begin{cases} e^{-\frac{\|\mathbf{y}_i-\mathbf{y}_j\|^2}{\sigma^2}} & \text{if} \quad \|\mathbf{y}_i - \mathbf{y}_j\|_2^2 < 2\boldsymbol{\sigma} \\ 0 & \text{else} \end{cases} \tag{29}$$

where σ is a parameter that is dependent on the maximum curvature on the manifold. The comparisons of the manifold regularized recovery scheme with low-rank and two-step PSF methods in Fig.(12) demonstrates the improved performance of this scheme. The interested readers are referred to [69, 70] for details.
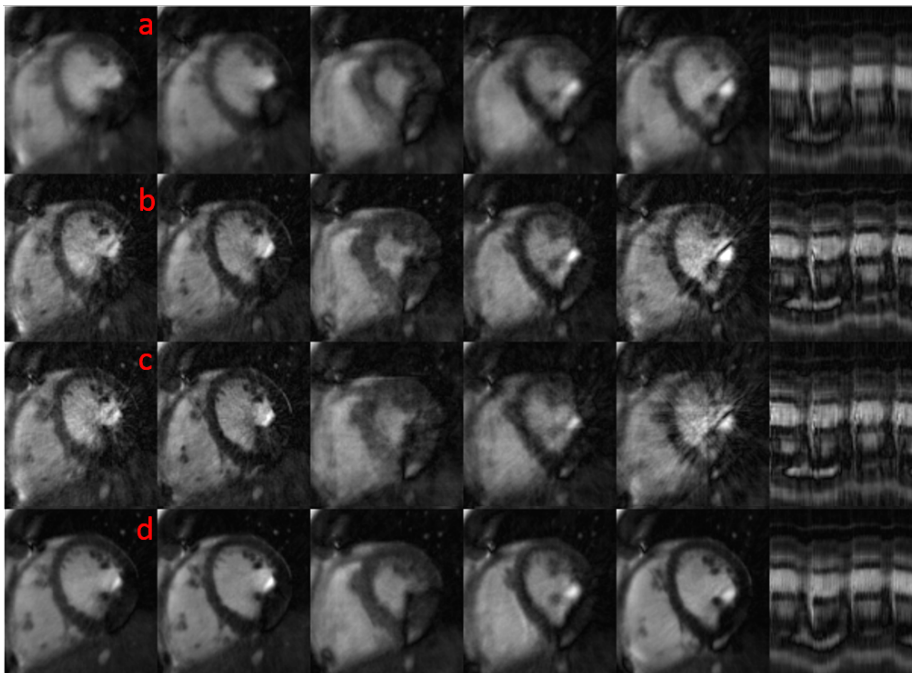

Figure 12: Reconstructions of free breathing & ungated CINE data using different algorithms: The rows correspond to reconstructions obtained using **(a)** Nuclear Norm minimization **(b)** Two-step PSF recovery **(c)** PSF with spatial TV regularization **(d)** Recovery using the manifold regularization specified by (28). The first five columns are representative images from the time series (cropped to include only the myocardium), while the last column shows the temporal intensity profile of the reconstructions along a vertical line.

0.7.2 Patch manifold regularization: application to implicit motion compensated dynamic MRI

The manifold structure of image patches has been widely used in image processing for denoising. These non-local regularization/smoothing schemes denoise

each patch in the image γ by expressing it as a weighted linear combination of other patches that are similar to it in the same image [71]. The weights $w_{x,y}$ between patches $P_x(\gamma)$ and $P_y(\gamma)$ centered at pixels x and y respectively are estimated as

$$\mathbf{w}_{x,y} = e^{-\frac{\|\mathbf{P}_x(\gamma) - \mathbf{P}_y(\gamma)\|^2}{\sigma^2}} \tag{30}$$

One of the difficulties in applying the classical non-local regularization scheme to MRI recovery from undersampled data had been the dependence of the criterion on pre-specified weights; the use of the weights estimated from aliased images often preserve the alias patterns rather than suppressing them. Some authors have shown that alternating between the denoising and weight-estimation step improves the quality of the images in deblurring applications [72], but often had limited success in heavily undersampled Fourier inversion problems. This alternating scheme for NLM has been recently shown to be equivalent to a majorize-minimize (MM) algorithm to optimize a regularized global cost function, where the regularization term is the sum of unweighted robust distances between image patches [73, 74]. The formulation as the optimization of a global criterion enabled the use of efficient continuation strategies to overcome the local minima problems. A fast iterative shrinkage algorithm was also introduced to solve the resulting regularization functional [75].

This patch regularization scheme has been recently demonstrated in dynamic MRI to obtain motion compensated recovery without explicit motion estimation. Fig.(13) illustrates the idea of implicit motion compensation. Small spatial patches are defined in an image frame, and similar patches are searched in a localized spatio-temporal neighborhood in subsequent time frames. Redundancies amongst the similar patches are then exploited. The recovery of such schemes can be posed as a regularized reconstruction scheme, where the non-local regularization penalty is an unweighted sum of distances between image patch pairs in the DMRI dataset:

$$\gamma^* = \arg \min_{\gamma(\mathbf{r},t)} \|\mathcal{A}(\boldsymbol{\gamma}) - \mathbf{b}\|_2^2 + \lambda \sum_{\mathbf{r}} \sum_{y \in \mathcal{N}(\mathbf{r})} \phi\left(P_x(\gamma) - P_y(\gamma)\right); \tag{31}$$

where $P_x(\gamma)$ is an image patch centered at the voxel x, and $N(x)$ indicates the small search neighborhood around x; ψ denotes a distance metric that saturates with distance to encourage smoothing between similar patches, while discouraging the averaging of dissimilar patches (see Fig.(13) for example choices of the ϕ metric).

This implicit motion compensated recovery scheme is a good alternative to explicit ME-MC schemes described in the previous section. Specifically, the ME-MC scheme involves solving highly nonlinear, non convex optimization problems, making it susceptible to local minima solutions. Although heuristic continuation schemes have been employed [56, 57], the convergence of these schemes to a global solution is not guaranteed. The reconstruction time of the explicit ME/MC schemes also are often prohibitive due to the expensive motion estimation step. By contrast, the advantage of these implicit ME/MC

26

(a) Searching of similar patches within a spatio-temporal neighborhood
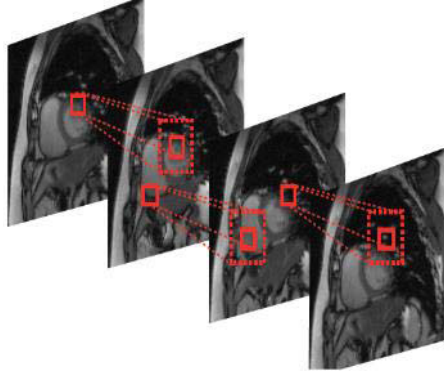
(b) Various choices of distance metric, ϕ
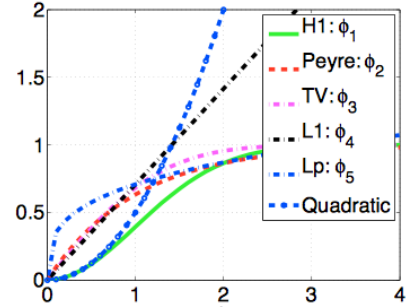
(c) Undersampled free breathing ungated cardiac cine MRI reconstruction

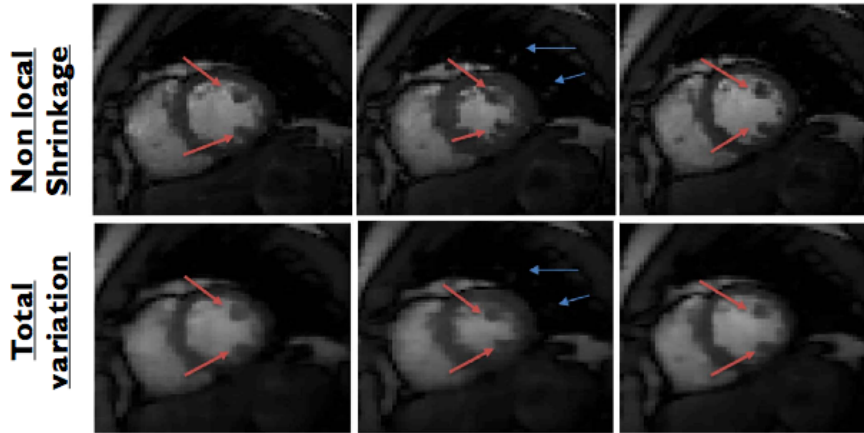Non local Shrinkage

Total variation

Figure 13: Implicit motion compensated reconstruction using non-local regularization: Similarity amongst small spatial patches within small spatio-temporal neighborhoods are exploited. The penalty in non-local regularized recovery is an unweighted sum of distances between patch pairs in the 3-D dataset. For a specified image patch, the penalty term involves the distances between itself and other patches in its cube shaped neighborhood. The robust distance metric is capable of exploiting the redundancy between similar patches, while excluding the dissimilar patches from averaging (different choices of this metric is shown in (b)). In (c), this scheme is used to recover under sampled ungated free breathing cardiac cine data, and its performance is compared against a spatio-temporal total variation regularized scheme.

schemes are its largely reduced computational complexity in comparison to explicit ME/MC schemes. For instance, the scheme by [75] has the computational complexity of a total variation regularized recovery scheme, but with greatly improved spatio-temporal fidelity due to implicit motion compensation (also

27

see Fig. 13).

Similar work in this area that capitalize on rank deficiency of the patches along an implicitly searched motion trajectory has also been proposed in [76] with good results. The implicit motion compensation offered by such manifold priors are expected to considerably advance dynamic MRI.

0.8 Summary

As discussed in this chapter, a wide variety of adaptive reconstruction algorithms have been proposed to improve the state of the art and minimize the challenges in dynamic MR imaging. While these schemes have great potential to improve DMRI imaging trade-offs, there exists a current gap in translation of these techniques to the clinic. A challenge lies in quantifying the properties (such as SNR, resolution, artifacts) of the nonlinear reconstructions. Several of these reconstruction algorithms rely on multiple parameters; there exists a challenge to automatically reconstruction datasets with minimal human intervention of choosing these parameters. With the use of modern hardware support such as graphical processing units, the reconstruction of several of these nonlinear algorithms have greatly improved, few of which obtain close to real time reconstruction [77, 78].

While this chapter has been focussed solely on MRI applications, the proposed methods can also find applications in other dynamic applications including low-dose cardiac CT and nuclear imaging modalities.

0.9 Acknowledgements

Bibliography

[1] T. Niendorf, D. K. Sodickson, G. A. Krombach, and J. Schulz-Menger, "Toward cardiovascular mri at 7 t: clinical needs, technical solutions and research promises," *European radiology*, vol. 20, no. 12, pp. 2806–2816, 2010.

[2] J. P. Finn, K. Nael, V. Deshpande, O. Ratib, and G. Laub, "Cardiac mr imaging: State of the technology 1," *Radiology*, vol. 241, no. 2, pp. 338–354, 2006.

[3] M. Schär, S. Kozerke, S. E. Fischer, and P. Boesiger, "Cardiac ssfp imaging at 3 tesla," *Magnetic resonance in medicine*, vol. 51, no. 4, pp. 799–806, 2004.

[4] B. J. Wintersperger, S. B. Reeder, K. Nikolaou, O. Dietrich, A. Huber, A. Greiser, T. Lanz, M. F. Reiser, and S. O. Schoenberg, "Cardiac cine mr imaging with a 32-channel cardiac coil and parallel imaging: Impact of acceleration factors on image quality and volumetric accuracy," *Journal of magnetic resonance imaging*, vol. 23, no. 2, pp. 222–227, 2006.

[5] M. Fenchel, V. S. Deshpande, K. Nael, J. P. Finn, S. Miller, S. Ruehm, and G. Laub, "Cardiac cine imaging at 3 tesla: initial experience with a 32-element body-array coil," *Investigative radiology*, vol. 41, no. 8, pp. 601–608, 2006.

[6] N. Seiberlich, G. Lee, P. Ehses, J. L. Duerk, R. Gilkeson, and M. Griswold, "Improved temporal resolution in cardiac imaging using through-time spiral grappa," *Magnetic Resonance in Medicine*, vol. 66, no. 6, pp. 1682–1688, 2011.

[7] E. Bresch, Y.-C. Kim, K. Nayak, D. Byrd, and S. Narayanan, "Seeing speech: Capturing vocal tract shaping using real-time magnetic resonance imaging," *IEEE Signal Processing Magazine*, vol. 25, no. 3, pp. 123–132, 2008.

[8] S. Narayanan, K. Nayak, S. Lee, A. Sethy, and D. Byrd, "An approach to real-time magnetic resonance imaging for speech production," *Journal of the acoustical society of America*, vol. 115, no. 4, pp. 1771–1776, 2004.

[9] P. Gatehouse, D. Firmin, S. Collins, and D. Longmore, "Real time blood flow imaging by spiral scan phase velocity mapping," *Magnetic resonance in medicine*, vol. 31, no. 5, pp. 504–512, 1994.

[10] K. S. Nayak, J. M. Pauly, A. B. Kerr, B. S. Hu, and D. G. Nishimura, "Real-time color flow mri," *Magnetic resonance in medicine*, vol. 43, no. 2, pp. 251–258, 2000.

[11] A. Shankaranarayanan, O. P. Simonetti, G. Laub, J. S. Lewin, and J. L. Duerk, "Segmented k-space and real-time cardiac cine mr imaging with radial trajectories 1," *Radiology*, vol. 221, no. 3, pp. 827–836, 2001.

[12] K. S. Nayak, C. H. Cunningham, J. M. Santos, and J. M. Pauly, "Real-time cardiac mri at 3 tesla," *Magnetic resonance in medicine*, vol. 51, no. 4, pp. 655–660, 2004.

[13] Z.-P. Liang, "Spatiotemporal imaging with partially separable functions," in *Noninvasive Functional Source Imaging of the Brain and Heart and the International Conference on Functional Biomedical Imaging, 2007. NFSI-ICFBI 2007. Joint Meeting of the 6th International Symposium on*. IEEE, 2007, pp. 181–182.

[14] Z.-P. Liang, H. Jiang, C. P. Hess, and P. C. Lauterbur, "Dynamic imaging by model estimation," *International journal of imaging systems and technology*, vol. 8, no. 6, pp. 551–557, 1997.

[15] Y. Bresler, "Fast acquisition and sampling in mri: Introduction to time-sequential sampling of spatio-temporal signals," in *Biomedical Imaging, 2002. Proceedings. 2002 IEEE International Symposium on*. IEEE, 2002, pp. 713–716.

[16] N. Aggarwal, Q. Zhao, and Y. Bresler, "Spatio-temporal modeling and minimum redundancy adaptive acquisition in dynamic mri," in *Biomedical Imaging, 2002. Proceedings. 2002 IEEE International Symposium on*. IEEE, 2002, pp. 737–740.

[17] Y. Bresler, N. Aggarwal, and B. Sharif, "Patient-adaptive spatio-temporal mri: From paradigm to paradise and beyond," in *Biomedical Imaging: From Nano to Macro, 2007. ISBI 2007. 4th IEEE International Symposium on*. IEEE, 2007, pp. 980–983.

[18] N. Aggarwal and Y. Bresler, "Patient-adapted reconstruction and acquisition dynamic imaging method (paradigm) for mri," *Inverse Problems*, vol. 24, no. 4, p. 045015, 2008.

[19] B. Sharif, J. A. Derbyshire, A. Z. Faranesh, and Y. Bresler, "Patient-adaptive reconstruction and acquisition in dynamic imaging with sensitivity encoding (paradise)," *Magnetic Resonance in Medicine*, vol. 64, no. 2, pp. 501–513, 2010.

[20] B. Madore, G. H. Glover, N. J. Pelc *et al.*, "Unaliasing by fourier-encoding the overlaps using the temporal dimension (unfold), applied to cardiac imaging and fmri," *Magnetic Resonance in Medicine*, vol. 42, no. 5, pp. 813–828, 1999.

[21] J. Tsao, "On the unfold method," *Magnetic resonance in medicine*, vol. 47, no. 1, pp. 202–207, 2002.

[22] J. Tsao, P. Boesiger, and K. P. Pruessmann, "k-t blast and k-t sense: Dynamic mri with high frame rate exploiting spatiotemporal correlations," *Magnetic Resonance in Medicine*, vol. 50, no. 5, pp. 1031–1042, 2003.

[23] H. Jung, K. Sung, K. S. Nayak, E. Y. Kim, and J. C. Ye, "k-t focuss: A general compressed sensing framework for high resolution dynamic mri," *Magnetic Resonance in Medicine*, vol. 61, no. 1, pp. 103–116, 2009.

[24] H. Jung, J. Park, J. Yoo, and J. C. Ye, "Radial k-t focuss for high-resolution cardiac cine mri," *Magnetic Resonance in Medicine*, vol. 63, no. 1, pp. 68–78, 2010.

[25] M. Lustig, J. M. Santos, D. L. Donoho, and J. M. Pauly, "kt sparse: High frame rate dynamic mri exploiting spatio-temporal sparsity," in *Proceedings of the 13th Annual Meeting of ISMRM, Seattle*, vol. 2420, 2006.

[26] R. Otazo, D. Kim, L. Axel, and D. K. Sodickson, "Combination of compressed sensing and parallel imaging for highly accelerated first-pass cardiac perfusion mri," *Magnetic Resonance in Medicine*, vol. 64, no. 3, pp. 767–776, 2010.

[27] L. Feng, R. Grimm, K. T. Block, H. Chandarana, S. Kim, J. Xu, L. Axel, D. K. Sodickson, and R. Otazo, "Golden-angle radial sparse parallel mri: Combination of compressed sensing, parallel imaging, and golden-angle radial sampling for fast and flexible dynamic volumetric mri," *Magnetic resonance in medicine*, vol. 72, no. 3, pp. 707–717, 2014.

[28] R. M. Lebel, J. Jones, J.-C. Ferre, M. Law, and K. S. Nayak, "Highly accelerated dynamic contrast enhanced imaging," *Magnetic Resonance in Medicine*, vol. 71, no. 2, pp. 635–644, 2014.

[29] J. Liu, A. Lefebvre, M. O. Zenge, M. Schmidt, E. Mueller, and M. S. Nadar, "2d bssfp real-time cardiac cine-mri: compressed sensing featuring weighted redundant haar wavelet regularization in space and time," *Journal of Cardiovascular Magnetic Resonance*, vol. 15, no. Suppl 1, p. P49, 2013.

[30] G. Adluru, C. McGann, P. Speier, E. G. Kholmovski, A. Shaaban, and E. V. DiBella, "Acquisition and reconstruction of undersampled radial data for myocardial perfusion magnetic resonance imaging," *Journal of Magnetic Resonance Imaging*, vol. 29, no. 2, pp. 466–473, 2009.

[31] A. S. Gupta and Z. Liang, "Dynamic imaging by temporal modeling with principal component analysis," 2001, p. 10.

[32] C. Brinegar, Y.-J. Wu, L. M. Foley, T. K. Hitchens, Q. Ye, C. Ho, and Z.-P. Liang, "Real-time cardiac mri without triggering, gating, or breath holding," in *Engineering in Medicine and Biology Society, 2008. EMBS 2008. 30th Annual International Conference of the IEEE.* IEEE, 2008, pp. 3381–3384.

[33] H. Pedersen, S. Kozerke, S. Ringgaard, K. Nehrke, and W. Y. Kim, "k-t pca: Temporally constrained k-t blast reconstruction using principal component analysis," *Magnetic resonance in medicine*, vol. 62, no. 3, pp. 706–716, 2009.

[34] S. Biswas, S. Poddar, S. Dasgupta, R. Mudumbai, and M. Jacob, "Two step recovery of jointly sparse and low-rank matrices: theoretical guarantees," *IEEE International Symposia on Biomedical Imaging (ISBI)*, 2015.

[35] S. G. Lingala, Y. Hu, E. DiBella, and M. Jacob, "Accelerated dynamic mri exploiting sparsity and low-rank structure: kt slr," *Medical Imaging, IEEE Transactions on*, vol. 30, no. 5, pp. 1042–1054, 2011.

[36] E. J. Candès and B. Recht, "Exact matrix completion via convex optimization," *Foundations of Computational mathematics*, vol. 9, no. 6, pp. 717–772, 2009.

[37] B. Recht, M. Fazel, and P. A. Parrilo, "Guaranteed minimum-rank solutions of linear matrix equations via nuclear norm minimization," *SIAM review*, vol. 52, no. 3, pp. 471–501, 2010.

[38] J. P. Haldar and D. Hernando, "Rank-constrained solutions to linear matrix equations using powerfactorization," *Signal Processing Letters, IEEE*, vol. 16, no. 7, pp. 584–587, 2009.

[39] J. P. Haldar and Z.-P. Liang, "Spatiotemporal imaging with partially separable functions: A matrix recovery approach," in *Biomedical Imaging: From Nano to Macro, 2010 IEEE International Symposium on.* IEEE, 2010, pp. 716–719.

[40] Y. Hu, S. G. Lingala, and M. Jacob, "A fast majorize–minimize algorithm for the recovery of sparse and low-rank matrices," *Image Processing, IEEE Transactions on*, vol. 21, no. 2, pp. 742–753, 2012.

[41] J. D. Trzasko, "Exploiting local low-rank structure in higher-dimensional mri applications," in *SPIE Optical Engineering+ Applications.* International Society for Optics and Photonics, 2013, pp. 885 821–885 821.

[42] J. Trzasko, A. Manduca, and E. Borisch, "Local versus global low-rank promotion in dynamic mri series reconstruction," in *Proc. Int. Symp. Magn. Reson. Med*, 2011, p. 4371.

[43] V. Vitanis, R. Manka, D. Giese, H. Pedersen, S. Plein, P. Boesiger, and S. Kozerke, "High resolution three-dimensional cardiac perfusion imaging using compartment-based k-t principal component analysis," *Magnetic Resonance in Medicine*, vol. 65, no. 2, pp. 575–587, 2011.

[44] A. G. Christodoulou, S. D. Babacan, and Z.-P. Liang, "Accelerating cardiovascular imaging by exploiting regional low-rank structure via group sparsity," in *Biomedical Imaging (ISBI), 2012 9th IEEE International Symposium on.* IEEE, 2012, pp. 330–333.

[45] A. G. Christodoulou, H. Zhang, B. Zhao, T. K. Hitchens, C. Ho, and Z.-P. Liang, "High-resolution cardiovascular mri by integrating parallel imaging with low-rankand sparse modeling," *Biomedical Engineering, IEEE Transactions on*, vol. 60, no. 11, pp. 3083–3092, 2013.

[46] M. Akçakaya, T. A. Basha, S. Pflugi, M. Foppa, K. V. Kissinger, T. H. Hauser, and R. Nezafat, "Localized spatio-temporal constraints for accelerated cmr perfusion," *Magnetic Resonance in Medicine*, vol. 72, no. 3, pp. 629–639, 2014.

[47] S. G. Lingala, E. DiBella, G. Adluru, C. McGann, and M. Jacob, "Accelerating free breathing myocardial perfusion mri using multi coil radial k- t slr," *Physics in medicine and biology*, vol. 58, no. 20, p. 7309, 2013.

[48] A. Majumdar, "Improved dynamic mri reconstruction by exploiting sparsity and rank-deficiency," *Magnetic resonance imaging*, vol. 31, no. 5, pp. 789–795, 2013.

[49] B. Zhao, J. P. Haldar, A. G. Christodoulou, and Z.-P. Liang, "Image reconstruction from highly undersampled-space data with joint partial separability and sparsity constraints," *Medical Imaging, IEEE Transactions on*, vol. 31, no. 9, pp. 1809–1820, 2012.

[50] M. Fu, B. Zhao, C. Carignan, R. K. Shosted, J. L. Perry, D. P. Kuehn, Z.-P. Liang, and B. P. Sutton, "High-resolution dynamic speech imaging with joint low-rank and sparsity constraints," *Magnetic Resonance in Medicine*, 2014.

[51] S. G. Lingala and M. Jacob, "Blind compressive sensing dynamic mri," *Medical Imaging, IEEE Transactions on*, vol. 32, no. 6, pp. 1132–1145, 2013.

[52] Y. Wang and L. Ying, "Compressed sensing dynamic cardiac cine mri using learned spatiotemporal dictionary," *Biomedical Engineering, IEEE Transactions on*, vol. 61, no. 4, pp. 1109–1120, 2014.

[53] J. Caballero, D. Rueckert, and J. V. Hajnal, "Dictionary learning and time sparsity in dynamic mri," in *Medical Image Computing and Computer-Assisted Intervention–MICCAI 2012.* Springer, 2012, pp. 256–263.

[54] M. Usman, D. Atkinson, F. Odille, C. Kolbitsch, G. Vaillant, T. Schaeffter, P. G. Batchelor, and C. Prieto, "Motion corrected compressed sensing for free-breathing dynamic cardiac mri," *Magnetic resonance in medicine*, vol. 70, no. 2, pp. 504–516, 2013.

[55] H. Jung and J. C. Ye, "Motion estimated and compensated compressed sensing dynamic magnetic resonance imaging: What we can learn from video compression techniques," *International Journal of Imaging Systems and Technology*, vol. 20, no. 2, pp. 81–98, 2010.

[56] X. Chen, M. Salerno, Y. Yang, and F. H. Epstein, "Motion-compensated compressed sensing for dynamic contrast-enhanced mri using regional spatiotemporal sparsity and region tracking: Block low-rank sparsity with motion-guidance (blosm)," *Magnetic Resonance in Medicine*, vol. 72, no. 4, pp. 1028–1038, 2014.

[57] S. Lingala, E. DiBella, and M. Jacob, "Deformation corrected compressed sensing (dc-cs): A novel framework for accelerated dynamic mri." *IEEE transactions on medical imaging*, vol. 34, no. 1, p. 72, 2015.

[58] S. G. Lingala, M. Nadar, C. Chefd'Hotel, L. Zhang, and M. Jacob, "Unified reconstruction and motion estimation in cardiac perfusion mri," in *Biomedical Imaging: From Nano to Macro, 2011 IEEE International Symposium on.* IEEE, 2011, pp. 65–68.

[59] M. S. Asif, L. Hamilton, M. Brummer, and J. Romberg, "Motion-adaptive spatio-temporal regularization for accelerated dynamic mri," *Magnetic Resonance in Medicine*, vol. 70, no. 3, pp. 800–812, 2013.

[60] P. Kellman, C. Chefd'hotel, C. H. Lorenz, C. Mancini, A. E. Arai, and E. R. McVeigh, "High spatial and temporal resolution cardiac cine mri from retrospective reconstruction of data acquired in real time using motion correction and resorting," *Magnetic Resonance in Medicine*, vol. 62, no. 6, pp. 1557–1564, 2009.

[61] ——, "Fully automatic, retrospective enhancement of real-time acquired cardiac cine mr images using image-based navigators and respiratory motion-corrected averaging," *Magnetic Resonance in Medicine*, vol. 59, no. 4, pp. 771–778, 2008.

[62] M. S. Hansen, T. S. Sørensen, A. E. Arai, and P. Kellman, "Retrospective reconstruction of high temporal resolution cine images from real-time mri using iterative motion correction," *Magnetic Resonance in Medicine*, vol. 68, no. 3, pp. 741–750, 2012.

[63] M. J. Ledesma-Carbayo, P. Kellman, A. E. Arai, and E. R. McVeigh, "Motion corrected free-breathing delayed-enhancement imaging of myocardial infarction using nonrigid registration," *Journal of Magnetic Resonance Imaging*, vol. 26, no. 1, pp. 184–190, 2007.

[64] H. Pedersen, H. Ólafsdóttir, R. Larsen, and H. B. Larsson, "A unifying model of perfusion and motion applied to reconstruction of sparsely sampled free-breathing myocardial perfusion mri," in *Biomedical Imaging: From Nano to Macro, 2010 IEEE International Symposium on.* IEEE, 2010, pp. 752–755.

[65] G. Adluru and E. V. DiBella, "Reconstruction with diffeomorphic motion compensation for undersampled dynamic mri," in *SPIE Optical Engineering+ Applications.* International Society for Optics and Photonics, 2013, pp. 88 581X–88 581X.

[66] J. B. Tenenbaum, V. De Silva, and J. C. Langford, "A global geometric framework for nonlinear dimensionality reduction," *Science*, vol. 290, no. 5500, pp. 2319–2323, 2000.

[67] V. D. Silva and J. B. Tenenbaum, "Global versus local methods in nonlinear dimensionality reduction," in *Advances in neural information processing systems*, 2002, pp. 705–712.

[68] M. Belkin and P. Niyogi, "Laplacian eigenmaps and spectral techniques for embedding and clustering." in *NIPS*, vol. 14, 2001, pp. 585–591.

[69] S. Poddar, S. G. Lingala, and M. Jacob, "Joint recovery of under sampled signals on a manifold: Application to free breathing cardiac mri," in *Acoustics, Speech and Signal Processing (ICASSP), 2014 IEEE International Conference on.* IEEE, 2014, pp. 6904–6908.

[70] S. Poddar and M. Jacob, "Low rank recovery with manifold smoothness prior: Theory and application to accelerated dynamic mri," *IEEE International Symposia on Biomedical Imaging (ISBI)*, 2015.

[71] Y. Lou, X. Zhang, S. Osher, and A. Bertozzi, "Image recovery via nonlocal operators," *Journal of Scientific Computing*, vol. 42, no. 2, pp. 185–197, 2010.

[72] G. Peyré, S. Bougleux, and L. Cohen, "Non-local regularization of inverse problems," in *Computer Vision–ECCV 2008.* Springer, 2008, pp. 57–68.

[73] Z. Yang and M. Jacob, "Nonlocal regularization of inverse problems: a unified variational framework," *Image Processing, IEEE Transactions on*, vol. 22, no. 8, pp. 3192–3203, 2013.

[74] ——, "Robust non-local regularization framework for motion compensated dynamic imaging without explicit motion estimation," in *Biomedical Imaging (ISBI), 2012 9th IEEE International Symposium on.* IEEE, 2012, pp. 1056–1059.

[75] Y. Mohsin, G. Ongie, and M. Jacob, "Iterative shrinkage algorithm for patch-smoothness regularized medical image recovery," *IEEE transactions on medical imaging*, 2015, early view.

[76] H. Yoon, K. Kim, D. Kim, Y. Bresler, and J. Ye, "Motion adaptive patch-based low-rank approach for compressed sensing cardiac cine mri." *IEEE transactions on medical imaging*, vol. 33, no. 11, p. 2069, 2014.

[77] M. Murphy, M. Alley, J. Demmel, K. Keutzer, S. Vasanawala, and M. Lustig, "Fast-spirit compressed sensing parallel imaging mri: scalable parallel implementation and clinically feasible runtime," *Medical Imaging, IEEE Transactions on*, vol. 31, no. 6, pp. 1250–1262, 2012.

[78] M. S. Hansen and T. S. Sørensen, "Gadgetron: an open source framework for medical image reconstruction," *Magnetic Resonance in Medicine*, vol. 69, no. 6, pp. 1768–1776, 2013.